

# Dose reduction for cardiac CT using a registration-based approach

Marcin Wierzbicki

*Imaging Research Laboratories, Robarts Research Institute, 100 Perth Drive, P.O. Box 5015, N6A 5K8, London, Ontario, Canada and  
Department of Medical Biophysics, The University of Western Ontario, N6A 5C1, London, Ontario, Canada*

G rard M. Guiraudon

*Imaging Research Laboratories, Robarts Research Institute, 100 Perth Drive, P.O. Box 5015, N6A 5K8, London, Ontario, Canada and  
Canadian Surgical Technologies and Advanced Robotics (CSTAR), 339 Windermere Road, N6A 5A5, London, Ontario, Canada*

Douglas L. Jones

*Canadian Surgical Technologies and Advanced Robotics (CSTAR), 339 Windermere Road, N6A 5A5, London, Ontario, Canada and  
Departments of Physiology & Pharmacology and Medicine, The University of Western Ontario, N6A 5C1, London, Ontario, Canada*

Terry Peters

*Imaging Research Laboratories, Robarts Research Institute, 100 Perth Drive, P.O. Box 5015, N6A 5K8, London, Ontario, Canada and  
Department of Medical Biophysics, The University of Western Ontario, N6A 5C1, London, Ontario, Canada*

(Received 16 October 2006; revised 21 March 2007; accepted for publication 24 March 2007; published 4 May 2007)

Two reasons for the recent rise in radiation exposure from CT are increases in its clinical applicability and the desire to maintain high SNR while acquiring smaller voxels. To address this emerging dose problem, several strategies for reducing patient exposure have already been proposed. One method employed in cardiac imaging is ECG-driven modulation of the tube current between 100% at one time point in the cardiac cycle and a reduced fraction at the remaining phases. In this paper, we describe how images obtained during such acquisition can be used to reconstruct 4D data of consistent high quality throughout the cardiac cycle. In our approach, we assume that the mid-diastole (MD) phase is imaged with full dose. The MD image is then independently registered to lower dose images (lower SNR) at other frames, resulting in a set of transformations. Finally, the transformations are used to warp the MD frame through the cardiac cycle to generate the full 4D image. In addition, the transformations may be interpolated to increase the temporal sampling or to generate images at arbitrary time points. Our approach was validated using various data obtained with simulated and scanner-implemented dose modulation. We determined that as little as 10% of the total dose was required to reproduce full quality images with a 1 mm spatial error and an error in intensity values on the order of the image noise. Thus, our technique offers considerable dose reductions compared to standard imaging protocols, with minimal effects on the quality of the final data.   2007 American Association of Physicists in Medicine. [DOI: [10.1118/1.2731030](https://doi.org/10.1118/1.2731030)]

Key words: CT dose reduction, x-ray tube current modulation, image registration

## I. INTRODUCTION

Due to recent technological advances and the resulting increases in clinical use, CT has become the leading manmade contributor to radiation exposure of the population.<sup>1</sup> In Canada, the number of CT studies performed annually has increased from 22 (1985–1990) to 41 (1991–1996) per 1000 people, while in the United States, the increase was from 14.5 (1980–1984) to 91 (1991–1996) per 1000 people.<sup>2,3</sup> As shown by Brix *et al.*,<sup>4</sup> the dose from a single CT scan may also be on the rise. One reason for this is that modern multislice scanners often do not make use of the penumbra during image acquisition. This affects the *z*-axis geometric efficiency, and hence the dose needed to acquire the image. The effect may be as little as 10% additional dose compared to a single slice scanner, but a doubling or more may be required

for multislice scanners with few slices and certain collimation widths.<sup>5</sup> Furthermore, helical reconstruction algorithms rely on interpolation, and thus require the acquisition of data outside the volume of interest. The amount of additional dose contributed by this “overscan” rises with the number of detector rows and decreases with increasing reconstructed image width.<sup>6</sup> Finally, although the drive towards smaller voxel sizes has resulted in exquisite image detail, more radiation exposure is required to maintain the same signal to noise ratio (SNR). With the continuing development of CT, radiation dose is likely to become an even larger problem requiring parallel advancements in technologies and guidelines that address this issue.<sup>7</sup>

Several strategies for dose reduction in CT imaging have already been proposed. One important method is to decrease

x-ray tube current as much as possible without affecting the clinical value of the final data. For example, Karla *et al.*<sup>8</sup> showed that only 50% of the dose may be required if the tube current is based on the patient's cross section. Similarly, Cohnen *et al.*<sup>9</sup> demonstrated that larger colorectal polyps (>5 mm) can be detected reliably even when the tube current has been significantly reduced. Dose also can be modified during image acquisition by modulating the x-ray tube current based on the patient/scanner geometry. This method is referred to as automatic exposure control, where the dose is reduced for specific rotation angles and slice locations to maintain the same quantum noise level in the projections. A recent study showed that one variation of this approach might reduce the dose by 10%–60% for children,<sup>10</sup> while the use of a similar algorithm was responsible for a 32% reduction in dose in 87% of the scans.<sup>11</sup> In cardiac CT, radiation exposure also can be physiologically gated to reduce dose. For example, Jakobs *et al.*<sup>12</sup> describe how the ECG signal, normally used to synchronize data acquisition with the heart, can be used to control the modulation of tube current between 100% at diastole and 20% elsewhere. A full quality image of the heart at diastole can then be reconstructed even though the overall dose has been reduced by up to 50%.

One limitation of the ECG-modulated approach of Jakobs *et al.* is that full quality images can only be reconstructed when 100% of the dose was used (e.g., diastole). Our goal is to build on this method and recover high SNR and artefact-free images throughout the cardiac cycle, despite the low quality of the data acquired at phases other than diastole. For this purpose, we use an image processing approach that also allows extraction of data at additional arbitrary time points in the cardiac cycle. We aim to reduce radiation dose to the patient and allow routine acquisition of high quality CT images for diagnosis of heart disease, validation of procedures, etc. Our ultimate goal is to use these images to build patient-specific geometry models for planning and guidance of minimally invasive cardiac surgery.

The dose-reduction approach presented in this manuscript involves the use of deformable registration for extraction of cardiac motion from a 4D image. Such methods have already been investigated by a number of researchers. Klein *et al.*<sup>13</sup> for example, treat the image volume as a physical elastic material. The motion of the heart is then estimated by calculating a set of transformations that are consistent between two different registration strategies. The authors suggest that the resulting motion can be used in improving gated cardiac PET images. Alternatively, Lorenzo-Valdés *et al.*<sup>14</sup> use a well-known registration algorithm<sup>15</sup> to describe the motion of the heart between the end-diastole frame and any other frame in a 4D image. Their goal is to automate the process of segmenting the left and right ventricles from dynamic MR data. Shen *et al.*<sup>16</sup> have devised a method to estimate the entire motion of the heart in one optimization procedure. This is achieved by ensuring that the transformations (motion) between frames of a 4D image are consistent in the forward and inverse directions, and that they are smooth in the spatial and temporal domains. Another example of a

method for extracting cardiac motion from 4D images is the work of Montagnat and Delingette.<sup>17</sup> They treat the problem using a 4D deformable model that is fitted to a 4D image using internal and external forces. The internal force ensures that the model remains smooth in the spatial and temporal domains, while the external force attracts the model to the boundaries of the left ventricle in MR images. Our deformable registration algorithm for motion extraction is described in more detail in Sec. II B.

## II. METHODS

We generate high quality, low total dose, 4D CT images of the heart using a three-step process. First, the data are acquired using a dose modulation approach similar to that described by Jakobs *et al.*<sup>12</sup> The data are then sorted according to their positions in the cardiac cycle and used to reconstruct an initial 4D data set, comprising a high quality (low noise) volumetric image at mid-diastole (MD frame), and lower quality frames at the remaining phases. The MD frame is then aligned with each of the low quality frames using our nonrigid registration algorithm, and a series of vector fields is calculated.<sup>18</sup> Consequently, the vector fields are used to deform the MD frame throughout the cardiac cycle to obtain the high quality 4D image. In addition, the vector fields may be interpolated to compute frames at arbitrary time points within the cardiac cycle.

In our approach, we assume that the quasistatic MD frame, having relatively few motion artefacts while at the same time being the most representative of the average heart shape, is the most suitable frame for animation over the entire cardiac cycle. We also assume that motion can be accurately extracted from the initial 4D data set, despite the low SNR of frames other than MD. The validity of this assumption was tested in a series of experiments (Sec. II D) approved by the University of Western Ontario Animal Ethics Review Board.

Our registration and interpolation approach is similar to that described for respiratory motion by McClelland *et al.*,<sup>19</sup> who acquire a high quality reference image during a breath hold to eliminate most artefacts related to respiration. The resulting image is then registered to 4D data acquired during free breathing. Thus, the high quality reference is animated throughout respiration and the artefacts due to motion and inconsistencies over the cycle are reduced (“averaged”). In this manuscript we simultaneously consider cardiac motion and dose reduction—two distinct challenges requiring unique solutions.

### A. Data acquisition

We were not able to modify clinical equipment to fully implement our proposed low dose acquisition protocol. Instead, we used less ideal modulation capabilities already installed on the scanners to acquire comparable data. In addition, we simulated data obtained using the ideal imaging protocol from 100% dose images (Sec. II D 1). In the proposed approach, images are acquired in helical mode over one breath-hold. During scanning, the ECG is recorded and



FIG. 1. Data acquisition protocol showing prospective modulation of x-ray tube current (dose  $D$ ) between 100% at mid-diastole (MD) and a reduced fraction elsewhere. Following acquisition, the data are binned according to the ECG and reconstructed into one high SNR frame at MD and low SNR frames elsewhere.

used prospectively to modulate the tube current between 100% of the prescribed level around MD and a significantly reduced fraction elsewhere (Fig. 1). Reducing tube current reduces the dose to the patient.<sup>20</sup> However, reducing exposure introduces additional noise to the acquired data since SNR is proportional to the square root of the detected x-ray flux.<sup>21</sup> Thus, data acquired using our method would consist of low-noise projections around MD, and views with higher noise levels elsewhere in the cardiac cycle. Following acquisition, the data are binned according to the cardiac phase indicated by the ECG and reconstructed using the standard software available on the scanner workstation. The result is an initial 4D data set, comprising several 3D frames ( $F$ ) depicting the heart at equally spaced time points in the cardiac cycle ( $F=0$  is the low noise MD image,  $F=1, 2, \dots$  are images at other phases with considerably higher noise levels).

## B. Registration

The second step of our method was the registration of the MD frame to the remaining frames of the initial 4D data (Fig. 2). The algorithm used to extract the necessary transformations was described previously,<sup>18</sup> but a short summary is presented here for completeness. Registration was per-

formed using a free-form deformation (FFD) technique, where a grid of nodes overlapping the source image facilitates its alignment with the target image. Each of the nodes was assigned a vector describing the local deformation around that node. These vectors were determined by simultaneously minimizing the mean squared difference (MSD) between the source and target intensity values and the 3D bending energy of the FFD.<sup>22</sup> The MSD acts as the attraction term that aligns the images while the bending energy term ensures a smooth vector field is calculated. For improved robustness, several optimization iterations were performed as the spacing between vectors was decreased from 28, to 14, and finally, to 7 mm. Interpolation of the image intensities and of the FFD vector field was performed using linear interpolation.

As shown in Fig. 2, registration of MD to nonadjacent frames was always performed in two steps. First,  $F=0$  was aligned with the frame just preceding the target frame. The calculated transformation was used to warp the MD image and the result was then registered to the target frame. These steps were performed sequentially, starting with the simultaneous registration of MD to  $F=NF-1$  and  $F=1$ , then to  $F=NF-2$  and  $F=2$ , etc. (where  $NF$  is the number of frames). Thus, registration of MD to frames much later in the cardiac cycle (e.g., end-systole) was performed gradually to avoid the accumulation of potential errors when extracting large deformations. Once the transformations between MD and all frames were estimated, the MD image was warped through the cardiac cycle to produce a set of low-noise frames (final 4D image).

## C. Interpolation

Time domain interpolation can be used to generate frames at arbitrary time points, for example, to increase the temporal sampling in the final 4D image. This interpolation was performed on the vector fields calculated during registration (see Fig. 3). Typically, our acquired data consisted of ten frames, so nine vector fields were calculated. A tenth, null

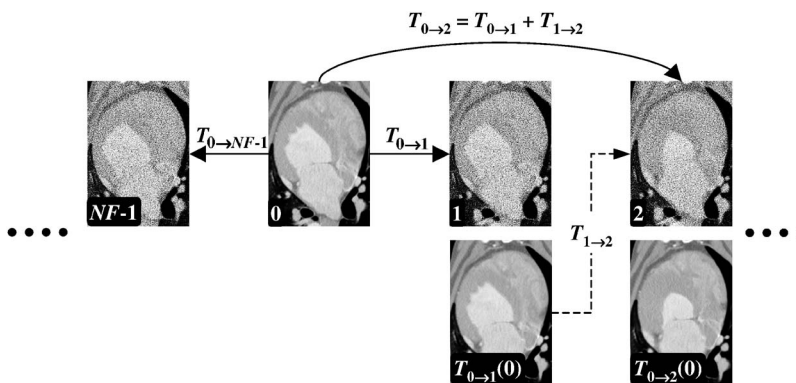


FIG. 2. Registration scheme used to extract the transformations between the MD image ( $F=0$ ) and the remaining frames (total number of frames= $NF$ ). The top row shows the reduced dose data and the bottom row shows the images obtained during registration. The right side of the diagram shows the registration of the MD image to frame 1. This was performed to obtain the transformation  $T_{0 \rightarrow 1}$ , which was then used to deform the MD image. The result, denoted as  $T_{0 \rightarrow 1}(0)$ , was then registered to frame 2 and the transformation  $T_{1 \rightarrow 2}$  was calculated (dashed arrow).  $T_{0 \rightarrow 1}$  and  $T_{1 \rightarrow 2}$  were concatenated (denoted as “+”) into a single transformation  $T_{0 \rightarrow 2}$  and the process was repeated. Simultaneously, the registration progresses in the other direction of the cardiac cycle starting with the alignment of the MD and  $NF-1$  frames (left side of diagram). Registration is complete once MD was registered to all frames.

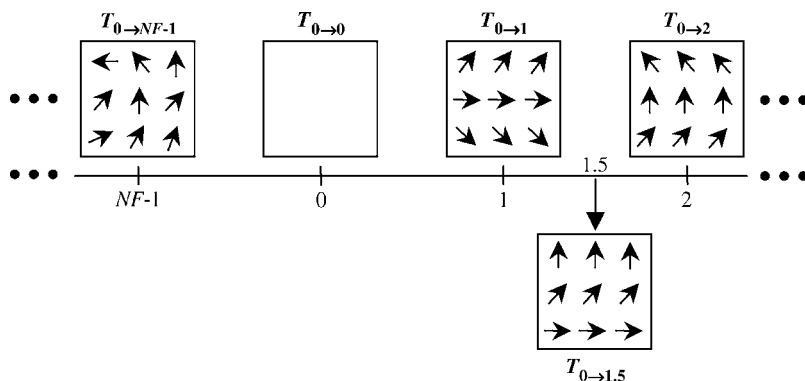


FIG. 3. Linear interpolation of the vector fields to allow the extraction of an image at an arbitrary time point in the cardiac cycle. In this example, the transformation to frame 1.5 is interpolated. The result is then used to deform the  $F=0$  image.

vector field was constructed to represent the deformation between the high quality MD image and itself. The ten transformations were then fitted with an interpolation function in the temporal direction. Finally, a new vector field for an arbitrary time point in the cardiac cycle was determined and used to warp the MD frame to that desired phase. We used linear interpolation of the vector fields since no improvements in results were observed when employing higher order methods.

#### D. Validation

Our approach was validated using a variety of images obtained from canine, porcine, and human subjects (Secs. II D 3, II D 4, and II D 5). However, we were not able to modify clinical equipment and fully implement our proposed low dose acquisition protocol. Instead, images were acquired using the less ideal tube current modulation schemes already available (e.g., the GE LightSpeed VCT scanner can acquire ECG-modulated images, but the minimum current is 20% of the maximum, and the length of time during which the current is reduced cannot be changed). In addition, we retrospectively simulated images obtained with the ideal modulation approach using 100% dose data (Sec. II D 1). Errors in extracting high quality images from these simulated or acquired low-dose data were measured as outlined in Sec. II D 2.

#### 1. Simulating modulation

As already stated, reducing dose increases the noise in the acquired images. Thus, to obtain our “simulated reduced dose” data, we decreased the SNR in frames other than MD in the images originally acquired without modulation. Since CT image noise originates mainly during the acquisition of projections, a process governed by photon counting statistics, the magnitude of noise in a CT image is<sup>21</sup>

$$\sigma \propto \frac{1}{\sqrt{NP}} \propto \frac{1}{\sqrt{Dose}} \propto \frac{1}{\sqrt{XI}}, \quad (1)$$

where  $\sigma$  is the noise,  $NP$  is the number of photons detected,  $Dose$  is the radiation dose, and  $XI$  is the tube current. However, Eq. (1) cannot be used to increase noise in a CT image on a voxel-by-voxel basis since the final CT noise is created by projection reconstruction, and thus is spatially correlated.

Instead, we generated a complete set of projections with Poisson distributed noise modeled using a Gaussian distribution with a mean value of 511, and standard deviation of 20 (simulating projections acquired with a photon-limited x-ray beam). A zero-mean “noise CT” image was then created by reconstructing the projections into a CT dataset<sup>23</sup> and subtracting the mean intensity value from each voxel.

For an original 4D image acquired without modulation, the SNR was then reduced in all frames other than MD by assuming CT noise to be additive,

$$I' = I + f_D \cdot NI, \quad (2)$$

where  $I'$  is the final image frame,  $I$  is the original frame obtained at 100% dose,  $NI$  is the noise image, and  $f_D$  is a parameter controlling the amount of noise added (and hence the simulated dose). The magnitude of  $f_D$  was determined using

$$\sigma' = \sqrt{\sigma^2 + (f_D \cdot \sigma_{NI})^2}, \quad (3)$$

where  $\sigma'$  is the noise in the final frame,  $\sigma$  is the noise in the original frame, and  $\sigma_{NI}$  is the noise level in the noise image itself. Noise was estimated by calculating the standard deviation of intensity values in a uniform region of interest (ROI). Combining Eqs. (1) and (3) gives

$$f_D = \frac{\sigma}{\sigma_{NI}} \sqrt{\frac{100}{D} - 1}, \quad (4)$$

where  $D$  is the fraction of the original dose ( $0 < D \leq 100\%$ ) simulated in the final image frame. Example re-

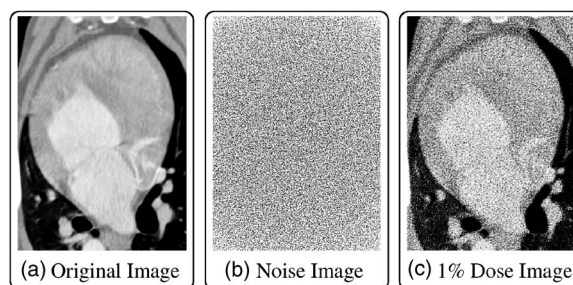


FIG. 4. Example axial slices from a canine image obtained when simulating a reduced dose acquisition. (a) Original frame with  $\sigma=20$  Hounsfield Units (HU); (b) noise image with  $\sigma_{NI}=10$  HU; (c) final frame with  $\sigma'=195$  HU (1% dose acquisition) obtained by setting  $f_D$  to 18.7.

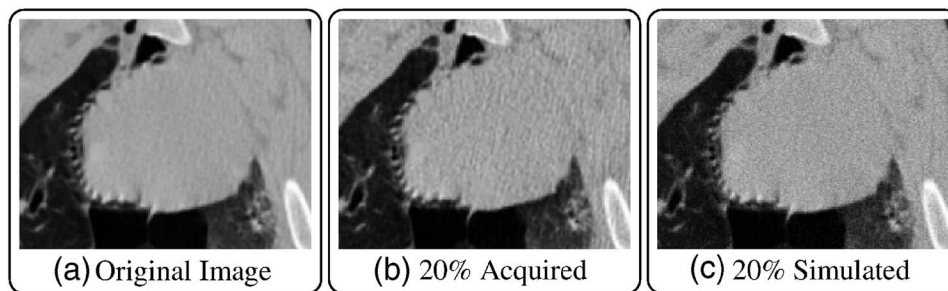


FIG. 5. Example axial slices from a porcine image obtained when simulating reduced dose acquisition. (a) Frame acquired using 400 mA tube current; (b) frame acquired using 80 mA; (c) frame obtained when simulating an 80 mA acquisition from the 400 mA frame.

sults are shown in Fig. 4 and simulated noise is compared to actual noise in Fig. 5. The appearance of simulated and acquired noise is slightly different due to the different reconstruction algorithms used for noise generation and during image acquisition.

## 2. Measuring error

The accuracy of our method at a specific frame  $F$  was quantified by calculating “landmark,” “mesh,” and “image” errors. To calculate landmark error, several points of interest (fiducials, boundaries of tissues, etc.) were first selected on the MD image. These points were then mapped to frame  $F$  using the transformation  $T_{0 \rightarrow F}$  (FFD vector field) and then compared to the expected locations at  $F$  (discrepancies were expressed as the RMS Euclidean distance). The approach to calculate mesh error was identical, except that a regular mesh of points (same geometry as the FFD grid) throughout the image volume was deformed. Thus, the mesh calculation was used to quantify spatial errors throughout the image volume. Finally, image error was obtained by deforming the MD image using  $T_{0 \rightarrow F}$  and calculating the mean absolute difference (MAD) between CT numbers in the warped image  $T_{0 \rightarrow F}(0)$  and the expected values at frame  $F$ . A gold standard for measuring any of the three errors was obtained using the methods presented in the next sections.

## 3. Canine data

Images of normal canine hearts were acquired on a GE LightSpeed Plus CT scanner without modulating the dose. The animals were anesthetized, paralyzed, and artificially ventilated to minimize artefacts due to breathing, while intracardiac contrast was enhanced by an intravenous injection of a contrast agent bolus. Each acquisition was performed in helical mode using 120 kVp, 200 mA x-rays, and a rotation time of 0.5 s for a total scan time of 30 s. The ECG recorded during imaging was used to retrospectively bin projections and 4D data were reconstructed with  $0.35 \times 0.35 \times 1.25 \text{ mm}^3$  voxels. Each 4D image comprised ten 3D frames ( $F=0, 1, \dots, 9$ ) equally spaced within the R-R interval. The length of this interval was set by the subjects’ heart rates which ranged from 70 to 85 bpm. In total, four datasets from three dogs were obtained (one dog was scanned twice on different days).

To simulate dose-modulated acquisitions, the data were combined with “noise images” as described above. In total, eleven 4D images were created for each of the four original data sets, each with frame  $F=0$  at 100% and the remaining frames at 100%, 50%, 40%, 30%, 20%, 10%, 8%, 6%, 4%, 2%, and 1% of the original dose. For all data sets, high quality representations were then recovered using the registration technique. In addition, even and then odd frames were eliminated from the registration procedure and the data at the missing frames were recovered using interpolation.

Results obtained using the 100% dose data were used as the gold standards when quantifying error. Thus, for a particular frame  $F$ , landmark and mesh errors were calculated by comparing locations of points obtained in the reduced dose frame (with or without interpolation) with those obtained in the full dose frame, while image errors were calculated by comparing the CT numbers of the two volumes. For landmark error calculations, we used points on the epicardial surface, which was manually segmented in the MD image of each subject as explained previously.<sup>18</sup>

## 4. Porcine data

Prior to imaging, CT-visible fiducials were placed on the pig’s beating epicardium to allow accurate tracking of heart motion, providing us with an independent gold standard against which we would validate our method. The markers were indirectly attached to the heart using a tubular nylon bandage retainer (BurnNet, Source Medical Corporation, Mississauga, Canada). Prior to surgery, a 5 cm diameter BurnNet tube was cut to a length of approximately 8.5 cm.

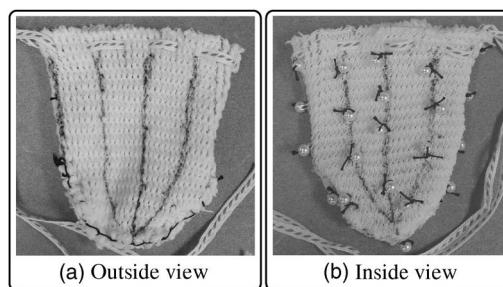


FIG. 6. BurnNet bandage retainer used to attach fiducials on the *in vivo* porcine heart. (a) Outside view; (b) inside out view (showing the plastic bead fiducials).

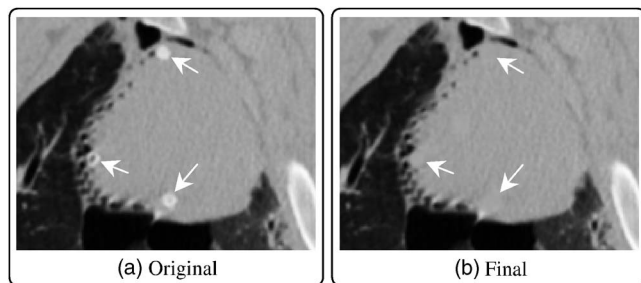


FIG. 7. Corresponding axial slices through the MD porcine image obtained before (a) and after (b) the removal of high intensity signal from the plastic fiducials (arrows).

One end was sutured closed forming a pocket, while the other end was threaded with umbilical tape (Ethicon, Peterborough, Canada) [Fig. 6(a)]. A total of 32, 4 mm diameter, plastic beads were then sutured to the inside of the pocket as shown in Fig. 6(b). Access to the heart was gained through a median sternotomy and an incision in the pericardial sack. The net was slipped over the heart from the apex and several sutures and the umbilical tape were used to hold the net in place. Before closing the pericardial sack and sternotomy, we used visual inspection to ensure that heart motion was unrestricted and that the fiducials remained in place with respect to the heart wall.

Postoperative images of the anesthetized pig were acquired using a GE LightSpeed VCT scanner running in helical mode during arrested breathing. The beam energy, slice thickness, and rotation time were 120 kVp, 0.625 mm, and 0.35 s respectively, for a total acquisition time of 7.6 s. Three data sets were acquired by setting the tube current to different levels. The first was obtained at 400 mA (no modulation) resulting in a volume CT Dose Index ( $CTDI_{vol}$ ) of 59.9 mGy. For the second and third scans, the tube current was modulated between 400/80 mA and 200/40 mA, resulting in  $CTDI_{vol}$  of 42.1 mGy and 21.3 mGy, respectively. Each of the three data sets was then binned according to the ECG and reconstructed with  $0.49 \times 0.49 \times 0.625 \text{ mm}^3$  voxels to form ten 3D images equally spaced throughout the R-R interval. The length of this interval was set by the subject's heart rate, which was approximately 85 bpm. For the modulated data, a ROI was selected in the trachea and the standard deviation of intensities was used to determine that frames  $F=0, 1, 8, 9$  were obtained at 100% tube current, frames  $F=3, 4, 5, 6$  at a 20% tube current, and frames  $F=2, 7$  at a transition current.

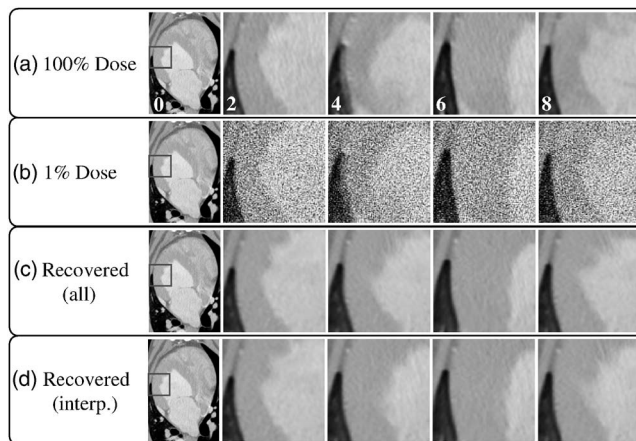


FIG. 8. Example axial slices from images of one canine subject. Original data (a), data obtained using simulated dose modulation (b), the results recovered using our method with all frames (c), and the results recovered with alternate frames and interpolation (d).  $F$  is indicated in white in the top row. Frames other than 0 are zoomed in as indicated by the boxes in the  $F=0$  results.

The 32 fiducials were then semiautomatically located in all frames of the 400, 400/80, and 200/40 mA images (beads were approximately 390 HU). The images were then processed to remove the high intensity signals from the beads to eliminate bias during registration. This was achieved by replacing voxel intensities around each landmark with random samples of water or air from elsewhere in the images (see Fig. 7).

The final processing step was to generate ten additional 4D data sets from the 400 mA scan to simulate our dose modulated acquisition. This was achieved by adding noise to frames 1–9 to simulate a dose of 50%, 40%, 30%, 20%, 10%, 8%, 6%, 4%, 2%, and 1% of the original. The resulting eleven 4D images (original data and the ten simulations) plus the two modulated acquisitions (400/80 and 200/40 mA) were then processed to extract full quality images. In addition, every odd and then every even frame were eliminated from the registration procedure and the data at the missing frames were interpolated.

Accuracy of results at any given frame, obtained with or without interpolation, was assessed by calculating landmark, mesh, and image errors. For the landmark error calculation, the landmark locations selected using the fiducial identification procedure outlined earlier were used as the gold standards. The gold standards for calculating mesh errors were the deformed meshes obtained using our method with the

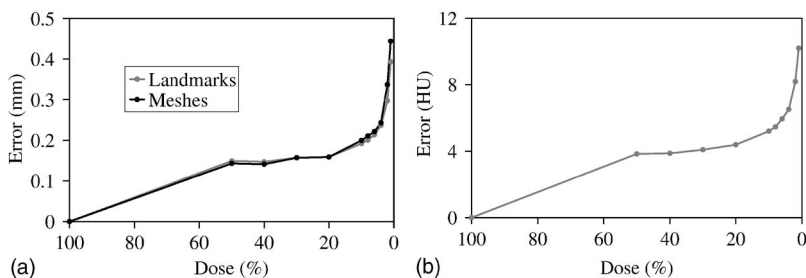


FIG. 9. Landmark, mesh (a), and image errors (b) obtained when recovering full quality canine images from data simulating reduced dose acquisitions. All values are the mean of the errors obtained at frames 1–9 averaged over the four subjects.

TABLE I. Landmark, mesh, and image errors at each frame obtained in the recovery of the full quality canine images from data simulating 1% dose acquisitions. All values are the mean±standard deviation of errors obtained over the four data sets.

Frame	Landmark error (mm)	Mesh error (mm)	Image error (HU)
1	0.2±0.0	0.1±0.0	6±1
2	0.2±0.0	0.2±0.0	8±1
3	0.4±0.0	0.4±0.1	11±0
4	0.5±0.1	0.6±0.2	13±1
5	0.7±0.2	0.8±0.2	14±1
6	0.6±0.3	0.7±0.2	13±1
7	0.5±0.3	0.6±0.2	12±1
8	0.3±0.1	0.4±0.1	9±1
9	0.3±0.2	0.2±0.1	7±1
Mean±STD	0.4±0.2	0.4±0.2	10±3

100% dose images (prior to removal of landmark signal from the images). Similarly, the gold standards for computing image errors were the deformed images obtained using our algorithm with the 100% dose data.

### 5. Human data

Human images, acquired using the Siemens SOMATOM Definition dual-source CT scanner, were provided by A.N. Primak and C.H. McCollough (CT Clinical Innovation Center, Mayo Clinic College of Medicine). The images were contrast-enhanced by injection of 100 cm<sup>3</sup> of Visipaque (320 mg/ml) at 5 cm<sup>3</sup>/s. The average heart rate of the subject was 49 bpm, resulting in an R-R interval length of approximately 1.22 s. The x-ray tube current was modulated during acquisition between 380 and 76 mAs (combined mAs from both tubes), with the higher current initiated approximately 0.24 s after each R-wave for approximately 0.73 s. Beam energy was held at 120 kVp and rotation time was 0.33 s, resulting in a combined CTDI<sub>vol</sub> of approximately 63.0 mGy. The acquired data were then binned according to the ECG signal and reconstructed with 0.39×0.39×0.75 mm<sup>3</sup> voxels. The resulting 4D image comprised 20 3D images equally spaced over the R-R interval. Thus, frames  $F=3, 4, 5, 6, 7, 8, 9$  were acquired with 20% of the dose used to acquire frames  $F=0, 1, 2, 10, \dots, 19$ .

Additional data sets were generated by reducing SNR in frames other than MD to simulate acquisitions with 20%, 10%, 8%, 6%, 4%, 2%, and 1% of the dose. For the 20% dose simulation, the original frames acquired at 20% of the dose ( $F=3, \dots, 9$ ) were not modified. The resulting eight 4D data sets (original acquisition and seven simulations) were then processed using our method to extract full quality images. In addition, every odd, and then every even frame were eliminated from the registration procedure, and the data at the missing frames were interpolated.

Accuracy was assessed by calculating landmark, mesh, and image errors. The gold standards were the deformed landmarks, meshes, and images obtained using our method with the original data. For the landmark error, specific points

TABLE II. Landmark, mesh, and image errors obtained in the recovery of the full quality canine images when 1% dose is simulated and only every other frame is used in the analysis (the missing frames are interpolated). All values are the mean±standard deviation of errors obtained over the four data sets.

Frame	Landmark error (mm)	Mesh error (mm)	Image error (HU)
0	0.2±0.0	0.2±0.1	8±2
1	0.5±0.1	0.4±0.1	15±2
2	0.3±0.0	0.3±0.0	10±1
3	0.5±0.1	0.5±0.2	14±2
4	0.9±0.2	0.7±0.1	19±4
5	1.2±0.2	0.9±0.1	18±2
6	0.8±0.2	0.8±0.2	16±1
7	0.6±0.1	0.6±0.1	15±2
8	0.4±0.0	0.4±0.1	12±2
9	0.5±0.1	0.4±0.0	15±2
Mean±STD	0.6±0.3	0.5±0.2	14±3

on the heart were selected by manually segmenting the epicardial and endocardial surfaces of the left ventricular myocardium.

## III. RESULTS

### A. Canine data

Figure 8 shows the ability of the registration algorithm to extract full quality images from canine data simulating lower dose acquisitions. Visually, there is very good agreement between the 100% dose images (row a) and our recovered data (rows c and d), despite the low quality of the input images (row b). Quantitatively, errors begin to increase when the dose in frames other than MD is reduced to ~5% (Fig. 9). However, Table I shows that even for a dose level of 1%, the landmark and mesh errors are still less than 1.0 mm (each frame) and the mean image error is 10±3 HU. Performing the analysis with every other frame and interpolating the

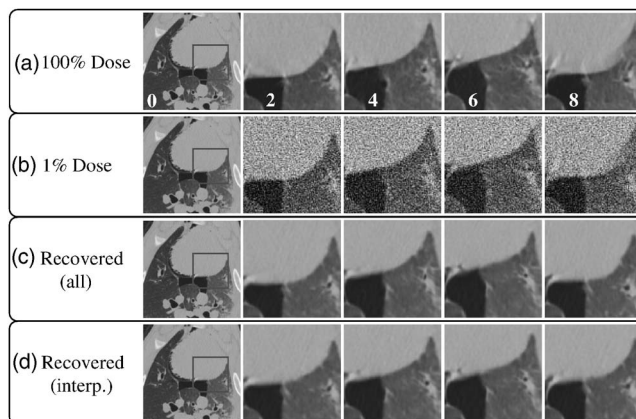


FIG. 10. Example axial slices from the porcine image. Original data (a), data obtained using simulated dose modulation (b), the results recovered using our method with all frames (c), and the results recovered with alternate frames and interpolation (d).  $F$  is indicated in white in the top row. Frames other than 0 are zoomed in as indicated by the boxes in the  $F=0$  results.

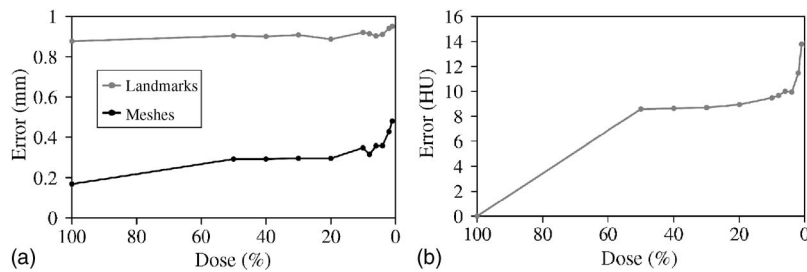


FIG. 11. Landmark, mesh (a), and image errors (b) obtained when recovering a full quality porcine image from data simulating reduced dose acquisitions. All values are the mean of the errors obtained at frames 1–9.

missing data (1% dose level) yields the results shown in Table II. As expected, these errors are slightly larger than those obtained when all frames are included, however, the mean landmark and mesh errors are still less than 1.0 mm, and the mean image error is only  $14 \pm 3$  HU. Other trends observed include higher errors around frame  $F=5$  and lower errors for frames near  $F=0$ . Also, we observed no significant differences between landmark and mesh errors.

### B. Porcine data

Example frames obtained with the porcine data are presented in Fig. 10. Again, there is very good agreement between the 100% dose images and our recovered data (compare row a to c and d). Quantitatively, landmark error rises only slightly over the dose levels simulated (Fig. 11). In contrast, the mesh and image errors increase when the dose in frames other than MD is reduced to  $\sim 5\%$ . However, Table III shows that mean landmark, mesh, and image errors are only  $1.0 \pm 0.3$  mm,  $0.5 \pm 0.2$  mm, and  $14 \pm 4$  HU respectively, even for a dose level of 1%. In comparison, the landmark errors obtained with the modulated 400/80 and 200/40 mA scans were  $0.9 \pm 0.4$  mm and  $0.8 \pm 0.3$  mm, respectively. Performing the analysis with every other frame and interpolating the missing data (1% dose level) yields the results shown in Table IV. The spatial errors are slightly larger than those obtained with all frames (mean landmark and mesh errors are  $1.1 \pm 0.3$  mm and  $0.5 \pm 0.1$  mm) but the mean image error has increased significantly from  $14 \pm 4$  to  $22 \pm 2$  HU ( $p < 0.01$ ). Other trends observed include a higher error level around frame  $F=4$  and lower errors for frames near  $F=0$ . Also,

TABLE III. Landmark, mesh, and image errors for each frame obtained in the recovery of the full quality porcine image from data simulating a 1% dose acquisition.

Frame	Landmark error (mm)	Mesh error (mm)	Image error (HU)
1	0.5	0.2	8
2	0.9	0.4	14
3	1.1	0.6	17
4	1.2	0.7	19
5	1.3	0.7	16
6	1.2	0.6	15
7	1.1	0.5	14
8	0.8	0.4	12
9	0.4	0.2	9
Mean $\pm$ STD	$1.0 \pm 0.3$	$0.5 \pm 0.2$	$14 \pm 4$

unlike the results obtained with the canine data, there is a significant difference between landmark and mesh errors (the former being approximately twice the latter).

### C. Human data

Figure 12 demonstrates our ability to generate full quality images from human data simulating a low dose acquisition (compare rows a to c and d). Quantitatively, errors begin to increase when the dose in frames other than MD is reduced to  $\sim 5\%$  (Fig. 13). However, Table V shows that mean landmark, mesh, and image errors are only  $0.6 \pm 0.4$  mm,  $0.6 \pm 0.3$  mm, and  $15 \pm 4$  HU, respectively, even for a dose level of 2%. Performing the analysis with every other frame and interpolating the missing data (2% dose level) yields the results shown in Table VI. As expected, these errors are larger than those obtained when all frames are included (mean landmark, mesh, and image errors are  $1.1 \pm 0.5$  mm,  $0.8 \pm 0.3$  mm, and  $25 \pm 6$  HU, respectively). Other trends observed include higher errors around frame  $F=10$ , and lower errors for frames near  $F=0$ . There were no significant differences between landmark and mesh errors.

## IV. DISCUSSION

In this manuscript, we presented a method for generating high quality 4D CT images of the heart from data acquired with reduced radiation dose. We validated our approach by analyzing canine, porcine, and human images obtained with scanner-implemented modulation, or through offline simula-

TABLE IV. Landmark, mesh, and image errors obtained in the recovery of the full quality porcine image when 1% dose is simulated and only every other frame is used in the analysis (the missing frames are interpolated).

Frame	Landmark error (mm)	Mesh error (mm)	Image error (HU)
0	0.4	0.3	17
1	1.0	0.4	23
2	1.2	0.4	21
3	1.2	0.6	23
4	1.3	0.6	22
5	1.3	0.6	24
6	1.3	0.7	23
7	1.3	0.7	24
8	0.8	0.5	21
9	0.9	0.5	23
Mean $\pm$ STD	$1.1 \pm 0.3$	$0.5 \pm 0.1$	$22 \pm 2$

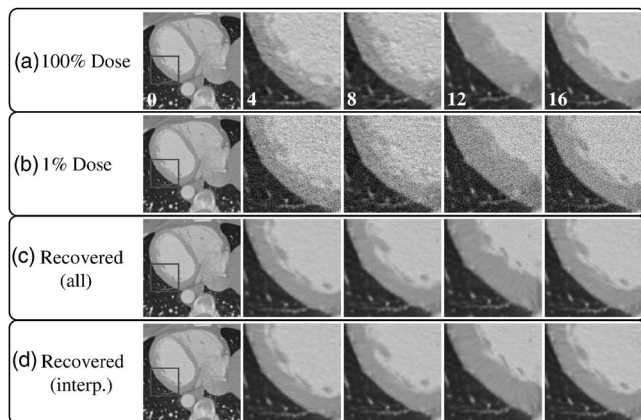


FIG. 12. Example axial slices from the human image. Original data (a), data obtained using simulated dose modulation (b), the results recovered using our method with all frames (c), and the results recovered with alternate frames and interpolation (d).  $F$  is indicated in white in the top row. Frames other than 0 are zoomed in as indicated by the boxes in the  $F=0$  results.

tions. Errors were quantified by comparing location of points and intensity values in the final images to the expected results.

Qualitative results from our validation are presented in Figs. 8, 10, and 12. We observed that a substantial amount of noise was added to the images when simulating modulated acquisitions (compare rows a and b). For frames other than MD, there was sufficient loss of contrast between regions, making boundary identification difficult. Using these low quality data as input, our algorithm produced the results shown in row c. The close agreement between rows a and c indicates that our approach is able to accurately recover full dose images from reduced dose data. Moreover, accuracy is not significantly affected even when every other frame is omitted from the analysis and the missing frames are interpolated (compare rows a and d).

Quantitative validation results are presented in Figs. 9, 11, and 13. We observed that errors in our method increase only once the dose in frames other than MD was reduced below  $\sim 5\%$ . In absolute terms, this translates to 15% of the original dose if ten frames are acquired (nine frames at 5% and one at 100%) and approximately 10% if 20 frames are acquired. Of course, these are theoretical values assuming that x-ray intensity can be modulated instantaneously between 100% and 5%. In practice, there would be a short delay, meaning that frames around MD would be acquired with higher dose. This would increase the final dose but improve the quality of data around MD, and hence, the accuracy of

TABLE V. Landmark, mesh, and image errors at each frame obtained in the recovery of the full quality human image from the data simulating a 2% dose acquisition.

Frame	Landmark error (mm)	Mesh error (mm)	Image error (HU)
1	0.2	0.2	8
2	0.3	0.2	10
3	0.3	0.3	12
4	0.4	0.5	14
5	0.5	0.6	15
6	0.6	0.6	16
7	0.6	0.7	17
8	0.9	0.8	18
9	0.9	1.0	20
10	1.3	1.1	21
11	1.2	1.0	21
12	1.1	0.9	20
13	1.0	0.8	19
14	0.7	0.7	17
15	0.5	0.6	15
16	0.4	0.4	14
17	0.3	0.4	13
18	0.3	0.3	11
19	0.2	0.2	8
Mean $\pm$ STD	0.6 $\pm$ 0.4	0.6 $\pm$ 0.3	15 $\pm$ 4

our approach. Another interesting observation from Figs. 9, 11, and 13 is the general agreement in trends across the data types, despite the fact that three different species were considered, and landmark errors were calculated on the surface of the epicardium and myocardium. The only similarities between data were voxel size ( $0.15 \text{ mm}^3$  canine and porcine,  $0.11 \text{ mm}^3$  human) and the noise level detected in the 100% dose, MD frames (standard deviation in a uniform ROI = 19 HU for canine, and 24 HU for porcine and human). Thus, the agreement of results suggests robustness of our method across different types of images.

In terms of specific trends, we observed a close agreement between landmark and mesh errors for canine [Fig. 9(a)] and human [Fig. 13(a)] data, indicating that the algorithm performs equivalently for specific locations on the heart and throughout the image volumes. In contrast, the landmark error is approximately twice the mesh error for porcine data [Fig. 11(a)]. This can be attributed to the lack of contrast agent (unavailable for this experiment) inside the porcine heart and its resulting uniform appearance. Epicardial surface motion can still be observed due to the differences in HU

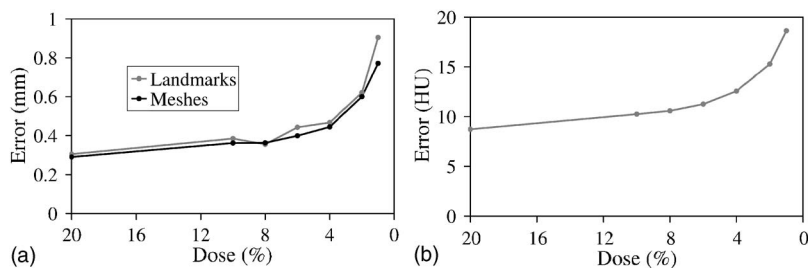


FIG. 13. Landmark, mesh (a), and image errors (b) obtained when recovering a full quality human image from data simulating reduced dose acquisitions. All values are the mean of the errors obtained at frames 1–19.

TABLE VI. Landmark, mesh, and image, errors obtained in the recovery of a full quality human image when 2% dose is simulated and only every other frame is used in the analysis (the missing frames are interpolated).

Frame	Landmark error (mm)	Mesh error (mm)	Image error (HU)
0	0.3	0.2	13
1	1.6	1.0	33
2	0.2	0.3	15
3	0.8	0.5	22
4	0.7	0.5	23
5	1.2	0.8	27
6	1.0	0.8	26
7	1.0	0.9	28
8	1.1	0.9	28
9	1.6	1.2	31
10	2.1	1.3	31
11	1.5	1.1	29
12	1.5	0.9	28
13	1.6	0.9	30
14	1.3	0.9	28
15	1.1	0.7	26
16	0.7	0.6	23
17	0.5	0.4	19
18	0.4	0.3	16
19	1.5	0.9	33
Mean±STD	1.1±0.5	0.8±0.3	25±6

between heart and lung tissue. Thus, landmark error is relatively high, since it is specific to the moving epicardium. On the other hand, mesh error is relatively low, since moving areas on the porcine epicardial surface and uniform areas that appeared to be static (due to a lack of contrast) inside the heart were considered in its calculation.

Other interesting trends in spatial errors were observed when comparing results from different data types. For example, at the 1% dose level, the mean landmark and mesh errors were  $0.4\pm 0.1$  and  $0.4\pm 0.1$  mm,  $1.0\pm 0.3$  and  $0.5\pm 0.2$  mm, and  $0.9\pm 0.5$  and  $0.8\pm 0.4$  mm for canine, porcine, and human data, respectively. Slightly larger errors were observed for human data for two reasons. First, the landmark and mesh locations used as gold standards for the human experiment were determined using an already dose-reduced data set (380/76 mAs modulation with  $F=3, \dots, 9$  acquired at  $\sim 76$  mA s), and were therefore less accurate than those obtained for the canine or porcine data. In addition, heart motion represented in the human images was more complex and larger in magnitude due to the acquisition of images with a dual source scanner (and the resulting reconstruction of 20 instead of 10 phases). Understandably, the larger the magnitude and complexity of the motion depicted in the images, the poorer the accuracy of the final data extracted using our algorithm. We also note from Fig. 11(a) that landmark error for the porcine data is  $0.9\pm 0.3$  mm for 100% dose images. As described in Sec. II D 4, this error was computed versus locations of plastic landmarks (independent gold standard). In contrast, the gold standards for canine and human data were the results obtained with 100% dose im-

ages. We can now estimate that the error in these imperfect “gold standards” is  $\sim 0.9\pm 0.3$  mm, meaning that errors calculated for the canine and human data may be slightly underestimated.

So far we have discussed spatial errors obtained with images generated using simulated dose modulation. We also tested our method with data acquired using online modulation available on the GE LightSpeed VCT scanner (porcine study). We found that the average landmark error was  $0.9\pm 0.4$  mm for the 400/80 mA scan ( $\text{CTDI}_{\text{vol}}=42.1$  mGy) and  $0.8\pm 0.3$  mm for the 200/80 mA scan ( $\text{CTDI}_{\text{vol}}=21.3$  mGy). By comparison, the error for the unmodulated acquisition was  $0.9\pm 0.3$  mm ( $\text{CTDI}_{\text{vol}}=59.9$  mGy). Even though the absolute dose was reduced to 70% and 35% for the 400/80 mA and 200/40 mA protocols, the resulting spatial error did not increase significantly. This indicates that practical implementation of our approach is possible and similar reductions in dose can be expected as in the simulated experiments.

Image errors follow trends that are similar to those observed for spatial errors. The smallest image errors were obtained with the canine data [Fig. 9(b)], followed by the porcine data [Fig. 11(b)], and finally the human data [Fig. 13(b)]. For the 1% dose level, the mean image errors were  $10\pm 1$ ,  $14\pm 4$ , and  $19\pm 5$  HU for the canine, porcine, and human images, respectively. This is a very good result, considering that the noise level in the canine, porcine, and human images at 100% dose was 19, 24, and 24 HU, respectively. The larger errors obtained with human data can be attributed to the reasons already discussed for spatial errors.

Errors obtained at different frames are presented in Table I (canine), Table III (porcine), and Table V (human), and as expected, they take their highest values at frames far away from MD due to the magnitude and complexity of the deformation to be extracted. However, errors are still relatively low even at end-systole ( $F=5$  for canine and porcine images, and  $F=10$  for the human data):  $0.7\pm 0.2$  mm landmark,  $0.8\pm 0.2$  mm mesh, and  $14\pm 1$  HU image (canine), 1.3 mm, 0.7 mm, and 19 HU (porcine), and 1.3 mm, 1.1 mm, and 21 HU (human). These results are excellent considering the voxel sizes and the original noise levels in the analyzed data. Errors increase when alternate frames are used in the analysis and the missing frames are obtained through interpolation (Tables II, IV, and VI). In general, a significant effect ( $p < 0.05$ ) is observed for all three image sets, but interpolation is especially difficult for the human data (2% dose level) where the mean landmark, mesh, and image errors increased from  $0.6\pm 0.5$  mm,  $0.6\pm 0.3$  mm, and  $15\pm 4$  HU, respectively (without interpolation) to  $1.1\pm 0.5$  mm,  $0.8\pm 0.3$ , and  $25\pm 6$  HU (with interpolation). Doubling of temporal resolution compared to the porcine or canine data means that more detailed vector fields need to be extracted, a difficult task if only half of the frames are available for analysis.

While we did not fully implement our data acquisition approach on a CT scanner, it is reasonable to assume that scan time would not be significantly increased compared to a standard imaging protocol. For the registration step, our

method required approximately 9 h for each canine or porcine 4D image, and 60 h for each human 4D image, using one Itanium 2 CPU running at 1.3 GHz. The interpolation of data took another 20 s per frame. The processing time depends mostly on the number of voxels considered, which was approximately 80, 160, and 900 million for each canine, porcine, and human 4D image, respectively. The software has not been optimized in any manner, so the current processing times are the maximums expected. Elsewhere in our laboratory, optimization of a similar nonrigid registration algorithm for the brain reduced the processing time for registration of a single volume from 8 h to less than 10 min,<sup>24</sup> and we believe that many of the same strategies can be employed here. For example, consider that originally, 48 and 254 min were required to achieve a registration error of 0.19 and 1.31 mm for target frames 1 and 10 of the human data (2% dose level). Performing the registration on a faster computer (AMD Athlon MP 2600+ with 1 GiB of memory) with the source and target images down sampled by a factor of 2 in each dimension reduced processing time to 5 and 23 min for frames 1 and 10 (error rose to 0.3 and 1.47 mm). Assuming that the above speed increases are constant for all frames, the processing time for the entire human 4D image would thus be reduced from 60 to ~6 h. Moreover, employing a simple multiprocessing strategy, where the two independent registrations (left and right directions in Fig. 2) are computed simultaneously, would reduce the current 6 h processing time to 3 h. We are confident that our future work on optimizing the code for specific hardware (as others in our group have done for brain registration) will significantly reduce this time further.

Through a series of validation experiments, we demonstrated that full quality images may be accurately generated from reduced dose data. Our technique involves tube current modulation during data acquisition and retrospective image processing to recover the high quality 4D images. A similar method, developed for respiratory motion imaging, was proposed by Li *et al.*<sup>25</sup> In their approach, low tube current was used throughout the respiratory cycle to acquire a 4D image with low SNR. The SNR of any frame  $F$  was then improved by co-registering all other frames to  $F$ , smoothing the resulting 4D intensity values using a penalized weighted least square function, and averaging the results. The resulting images have slightly reduced SNR compared to those obtained at full dose, but only 10% of the tube current is required during acquisition. Although developed for respiratory motion, this technique is equally applicable to cardiac imaging. A major advantage would be that modulation is not required during acquisition. However, having a full quality frame at MD is expected to improve intraframe registration and our ability to extract cardiac motion throughout the cycle. In addition, full exposure can also be used at a distant frame (e.g., end-systole) for further improvements in accuracy (specifically for registration of MD to end-systole). This motion can then be visualized by deforming a geometric model such as the surface of the left ventricle,<sup>18</sup> or as presented in this manuscript, deforming the MD frame. In addition, extracting accurate motion allows us to accurately interpolate additional

frames between those already available. Finally, if motion extraction cannot be performed, a full quality MD image will still be available for processing, diagnosis, and other applications.

We also note that the combination of the MD frame along with the set of transformations constitutes a form of dynamic image compression. For example, the original human data set requires a total of 1740 MB of disk storage for the full 20 frames (12-bit images, cropped to contain the heart only). In comparison, the disk space required to store the MD frame and 19 transformations obtained using our method is 106 MB. With continued progress towards smaller voxels and improved temporal resolution in cardiac CT, methods such as ours will become increasingly important in facilitating storage and transfer of big data sets.

## V. CONCLUSION

In this manuscript we presented a technique for recovering a full quality 4D CT image from data acquired with reduced dose over most of the cardiac cycle. In addition, a temporal interpolation method was introduced to allow extraction of frames in between those already available. Through several validation experiments, we demonstrated that this approach is robust over a range of data types, different regions of the heart, and with different levels of dose. We showed that total dose could be reduced to 10% (20 frame data), and images corresponding with 100% dose acquisitions could still be reconstructed accurately in terms of spatial and intensity-value correspondence. Aside from the dose reduction factor, errors in our method also depend on the amount of motion to be recovered from the source data. Thus, larger errors occur in high-motion areas of the heart such as the apex, particularly at frames far away from MD.

In the future, we plan to implement this technique on a commercial CT scanner, to optimize the image registration code, and to make use of special purpose hardware to significantly reduce processing time. It will then be important to re-evaluate the method in terms of the clinical usefulness of the images versus dose employed during acquisition. We expect the techniques described in this manuscript to facilitate the acquisition of high quality dynamic CT scans for both diagnosis and intervention planning and guidance.

## ACKNOWLEDGMENTS

The authors thank the animal technician team at St. Joseph's Hospital, London, Canada, especially Jane Sykes, for their assistance in performing the *in vivo* porcine experiments. We also express our gratitude to Aaron So for help with image acquisition, and Dr. A. N. Primak and Dr. C. H. McCollough of the Mayo Clinic for providing the human data. Finally, thank you to Chris Wedlake and John Moore for computer support and Atamai Inc. for visualization software. This work was supported by grants from the Canadian Institutes of Health Research (MOP 14735), Ontario Consortium for Image-guided Therapy and Surgery, Canadian Foundation for Innovation, Ontario Innovation Trust, Natural Sci-

ences and Engineering Research Council of Canada, and the University of Western Ontario.

- <sup>1</sup>M. K. Kalra, M. M. Maher, S. Rizzo, and S. Saini, "Radiation exposure and projected risks with multidetector-row computed tomography scanning: Clinical strategies and technologic developments for dose reduction," *J. Comput. Assist. Tomogr.* **28**, S46–S49 (2004).
- <sup>2</sup>UNSCEAR, *Sources and Effects of Ionizing Radiation* (United Nations, New York, 1993).
- <sup>3</sup>UNSCEAR, *Sources and Effects of Ionizing Radiation* (United Nations, New York, 2000), Vol. 1.
- <sup>4</sup>G. Brix, H. D. Nagel, G. Stamm, R. Veit, U. Lechel, J. Griebel, and M. Galanski, "Radiation exposure in multi-slice versus single-slice spiral CT: Results of a nationwide survey," *Eur. Radiol.* **13**, 1979–1991 (2003).
- <sup>5</sup>ImPACT, Radiation dose issues in multi-slice CT scanning (2005).
- <sup>6</sup>R. Nicholson and S. Fetherston, "Primary radiation outside the image volume of a multislice helical CT scan," *Br. J. Radiol.* **75**, 518–522 (2002).
- <sup>7</sup>S. J. Golding and P. C. Shrimpton, "Radiation dose in CT: Are we meeting the challenge?," *Br. J. Radiol.* **75**, 1–4 (2002).
- <sup>8</sup>M. K. Kalra, S. Prasad, S. Saini, M. A. Blake, J. Varghese, E. F. Halpern, J. T. Rhea, and J. H. Thrall, "Clinical comparison between standard dose and 50% reduced dose abdominal CT: Effect on image quality," *AJR, Am. J. Roentgenol.* **179**, 1101–1106 (2002).
- <sup>9</sup>M. Cohnen, C. Vogt, A. Beck, K. Andersen, W. Heinen, S. vom Dahl, V. Aurich, D. Haeussinger, and U. Moedder, "Feasibility of MDCT colonography in ultra-low-dose technique in the detection of colorectal lesions: Comparison with high-resolution video colonoscopy," *AJR, Am. J. Roentgenol.* **183**, 1355–1359 (2004).
- <sup>10</sup>H. Greess, A. Nömayr, H. Wolf, U. Baum, M. Lell, B. Böwing, W. A. Kalender, and W. A. Bautz, "Dose reduction in CT examinations of children by attenuation-based on-line modulation of tube current (CARE dose)," *Eur. Radiol.* **12**, 1571–1576 (2002).
- <sup>11</sup>M. K. Kalra, M. M. Maher, T. L. Toth, R. S. Kamath, E. F. Halpern, and S. Saini, "Comparison of z-axis automatic tube current modulation technique with fixed tube current CT scanning of abdomen and pelvis," *Radiology* **232**, 347–353 (2004).
- <sup>12</sup>T. F. Jakobs, C. R. Becker, B. Ohnesorge, T. G. Flohr, C. Suess, U. J. Schoepf, and M. F. Reiser, "Multislice helical CT of the heart with retrospective ECG gating: Reduction of radiation exposure by ECG-controlled tube current modulation," *Eur. Radiol.* **12**, 1081–1086 (2002).
- <sup>13</sup>G. J. Klein and R. H. Huesman, "Four-dimensional processing of deformable cardiac PET data," *Med. Image Anal.* **6**, 29–46 (2002).
- <sup>14</sup>M. Lorenzo-Valdés, G. I. Sanchez-Ortiz, R. Modiaddin, and D. Rueckert, "Atlas-based segmentation and tracking of 3D cardiac MR images using non-rigid registration," in *Medical Image Computing and Computer-Assisted Intervention (MICCAI) Tokyo, LNCS 2488* (Springer-Verlag, Berlin, 2002), pp. 642–650.
- <sup>15</sup>D. Rueckert, L. I. Sonoda, C. Hayes, D. L. G. Hill, M. O. Leach, and D. J. Hawkes, "Nonrigid registration using free-form deformations: Application to breast MR images," *IEEE Trans. Med. Imaging* **18**, 712–721 (1999).
- <sup>16</sup>D. Shen, H. Sundar, Z. Xue, Y. Fan, and H. Litt, "Consistent estimation of cardiac motions by 4D image registration," in *Medical Image Computing and Computer-Assisted Intervention (MICCAI) Palm Springs, LNCS 3750* (Springer-Verlag, Berlin, 2005), pp. 902–910.
- <sup>17</sup>J. Montagnat and H. Delingette, "4D deformable models with temporal constraints: Application to 4D cardiac image segmentation," *Med. Image Anal.* **9**, 87–100 (2005).
- <sup>18</sup>M. Wierzbicki, M. Drangova, G. Guiraudon, and T. M. Peters, "Validation of dynamic heart models obtained using non-linear registration for virtual reality training, planning, and guidance of minimally invasive cardiac surgeries," *Med. Image Anal.* **8**, 387–401 (2004).
- <sup>19</sup>J. R. McClelland, J. M. Blackall, S. Tarte, A. C. Chandler, S. Hughes, S. Ahmad, D. B. Landau, and D. J. Hawkes, "A continuous 4D motion model from multiple respiratory cycles for use in lung radiotherapy," *Med. Phys.* **33**, 3348–3358 (2006).
- <sup>20</sup>M. F. McNitt-Gray, "AAPM/RSNA physics tutorial for residents: Topics in CT. Radiation dose in CT," *Radiographics* **22**, 1541–1553 (2002).
- <sup>21</sup>R. A. Brooks and G. Di Chiro, "Statistical limitations in x-ray reconstructive tomography," *Med. Phys.* **3**, 237–240 (1975).
- <sup>22</sup>F. L. Bookstein, "Principal warps: Thin-plate splines and the decomposition of deformations," *IEEE Trans. Pattern Anal. Mach. Intell.* **11**, 567–585 (1989).
- <sup>23</sup>R. Fahrig, A. J. Fox, S. Lownie, and D. W. Holdsworth, "Use of a c-arm system to generate true three-dimensional computed rotational angiograms: Preliminary *in vitro* and *in vivo* results," *AJNR Am. J. Neuroradiol.* **18**, 1507–1514 (1997).
- <sup>24</sup>K. Finnis, Y. Starreveld, A. G. Parent, A. F. Sadikot, and T. M. Peters, "Three-dimensional database of subcortical electrophysiology for image-guided stereotactic functional neurosurgery," *IEEE Trans. Med. Imaging* **22**, 93–104 (2003).
- <sup>25</sup>T. Li, B. Schreiber, B. Thorndyke, G. Tillman, and A. Boyer, "Radiation dose reduction in four-dimensional computed tomography," *Med. Phys.* **32**, 3650–3660 (2005).